A two-dimensional axial-radial full-fluid moment model for Hall effect thrusters

IEPC-2025-382

Presented at the 39th International Electric Propulsion Conference, Imperial College London, London, United Kingdom
14-19 September 2025

Daniel E. Troyetsky[*], Elias Bögel[†] and Kentaro Hara[‡]
Stanford University, Stanford, CA, 94305, USA

Hall effect thruster (HET) simulations are typically performed using either fully-fluid methods (i.e., fluid electrons and ions), hybrid methods with kinetic heavy species and fluid electrons, or fully kinetic methods. For both fluid and hybrid models, the plasma is often assumed to be quasineutral, preventing the resolution of plasma sheaths which may be important for studying plasma-wall interactions and near-wall electron transport. The drift-diffusion approximation is usually made for fluid electrons, which neglects inertial effects, although recent work has suggested that these effects may be a contributing factor to cross-field electron transport. A two-dimensional axial-radial five-moment fluid model for electrons is developed which relaxes these assumptions. Ions are treated using a two-fluid five-moment model. A simplified quasi-steady model is used for neutrals. The results are compared to particle-in-cell Monte Carlo collision simulations, highlighting the advantages and limitations of five-moment fluid electron models for HETs compared with existing approaches.

I. Introduction

Hall effect thrusters (HETs) are low-temperature, partially-magnetized, E×B devices that operate in a transitional regime between kinetic and fluid descriptions. When modeling HETs, there is therefore a trade-off between computational cost and physical accuracy. Fluid formulations are typically less expensive, but require more assumptions to be made which may reduce model fidelity. Because of this, many of the most widely used models in the literature are hybrid models that utilize the drift-diffusion approximation for electrons, neglecting inertial effects and assuming that the electrons are at steady state with respect to the time scales of the heavier species.[1–3] These models are also often quasineutral, preventing the resolution of plasma sheaths.

Recent work has demonstrated that the drift-diffusion approximation is invalid when the kinetic energy of electrons is significant, which is the case in a closed-drift system such as a HET.[4] Additional studies using both one-dimensional fluid moment and fully kinetic models of a HET have shown that axial and azimuthal shear in the electron momentum equations can lead to enhanced cross-field transport, further invalidating the drift diffusion assumption.[5–7] Multi-dimensional kinetic simulations of HETs have demonstrated the importance of plasma-wave interactions in driving cross-field electron transport.[8,9] In addition to wave-driven electron transport, another proposed means of cross-field electron transport is via interactions with the walls, which cannot be self-consistently captured without resolving the plasma sheaths.[10,11]

In this study, a two-dimensional, axial-radial simulation of a HET is developed to study shear-induced and wall-induced cross-field electron transport, in a similar configuration to that of Ref. 12. The model solves the five-moment (5M) system of equations, i.e., conservation of mass, momentum, and energy, for electrons and ions and accounts for non-neutrality of the plasma. A multi-fluid approach is used for the ions accounting for separate high-energy and low-energy subpopulations.[13] A simplified one-dimensional

---

[*] PhD Candidate, Aeronautics and Astronautics, dtroyets@stanford.edu.
[†] Graduate Student, Aeronautics and Astronautics, bogel@stanford.edu.
[‡] Assistant Professor, Aeronautics and Astronautics, kenhara@stanford.edu.

neutral law is used in the discharge channel to accelerate convergence to steady state and is coupled to a collisionless steady-state plume model.[12,14] The 5M results are compared to particle-in-cell Monte Carlo collision (PIC-MCC) simulation results for verification and to assess the advantages and limitations of the proposed modeling approach.

II. Simulation setup

A schematic of the Hall effect thruster (HET) geometry is shown in Figure 1. The anode is a conducting material at fixed potential whereas the channel walls and pole pieces are dielectric materials. The plume is truncated in the near-field and the entire dashed line boundary is treated as the cathode electron emission plane. Both the five-moment (5M) fluid and particle-in-cell Monte Carlo collision (PIC-MCC) models are two-dimensional (2D) in space and solve for all three components of velocity (3V). Although cylindrical effects should be considered for a realistic HET model, a Cartesian assumption is made in this benchmarking study.

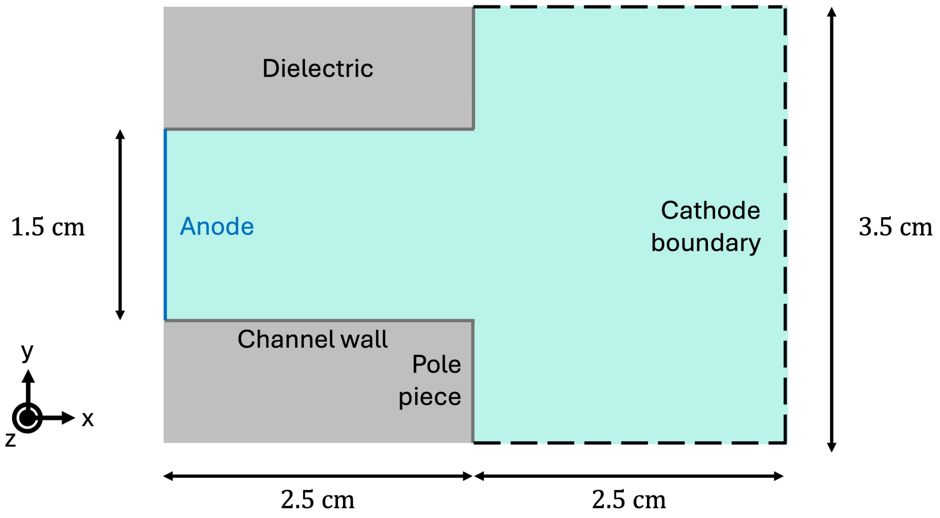

Figure 1. Schematic representation of the computational domain.

To reduce the computational cost, an augmented vacuum permittivity of $\epsilon_0' = f_\epsilon^2 \epsilon_0$ is used, which numerically increases the Debye length, $\lambda_D = (\epsilon_0' T_e / e n_e)^{1/2}$, and decreases the plasma frequency, $\omega_{pe} = (e^2 n_e / \epsilon_0' m_e)^{1/2}$, by a factor of f_ϵ, where T_e is electron temperature, n_e is electron density, e is the fundamental charge, and m_e is the electron mass. A value of $f_\epsilon = 10$ is used in this study.

The magnetic field is assumed to be purely in the radial direction and is given by

$$B_y(x) = B_0 \exp\left[-\left(\frac{x - L_{ch}}{\ell} \right)^2 \right], \tag{1}$$

where $B_0 = 150$ G, $\ell = 1.35$ cm if $x < L_{ch}$ and $\ell = 1.0$ cm if $x \geq L_{ch}$.

III. The five-moment fluid model

A hierarchy of fluid models can be derived by taking statistical moments of the Boltzmann equation,

$$\frac{\partial f}{\partial t} + \vec{v} \cdot \frac{\partial f}{\partial \vec{x}} + \vec{a} \cdot \frac{\partial f}{\partial \vec{v}} = \left. \frac{\delta f}{\delta t} \right|_{coll}, \tag{2}$$

where f is the velocity distribution function, t is time, $\vec{x}$ is particle position, $\vec{v}$ is particle velocity, $\vec{a}$ is particle position, and the right hand side is an instantaneous collision operator. In Cartesian coordinates, assuming an isotropic pressure tensor ($\bar{\bar{p}} = p\delta_{ij}$), the first five moments of Eq. (2) give the mass, momentum, and energy conservation equations:

$$\frac{\partial n}{\partial t} + \nabla \cdot (n\vec{u}) = \dot{n}, \tag{3}$$

$$\frac{\partial}{\partial t}(n\vec{u}) + \nabla \cdot \left(n\vec{u} \otimes \vec{u} + \frac{\bar{\bar{p}}}{m} \right) = \frac{qn}{m}\left(\vec{E} + \vec{u} \times \vec{B}\right) + \vec{C}, \tag{4}$$

$$\frac{\partial n\epsilon}{\partial t} + \nabla \cdot (n\epsilon\vec{u} + \bar{\bar{p}} \cdot \vec{u} + \vec{q}) = qn\vec{E} \cdot \vec{u} + \mathcal{C}, \tag{5}$$

where n is number density, $\vec{u}$ is velocity, $\dot{n}$ is the particle source term, $\bar{\bar{p}}$ is the pressure tensor, m is mass, q is charge, $\vec{E}$ is the electric field, $\vec{B}$ is the magnetic field, $\vec{C}$ is the momentum contribution due to collisions, ϵ is mean energy, $\vec{q}$ is the conductive heat flux, and $\mathcal{C}$ is the energy source term due to inelastic collisions. It is further assumed that the fluid behaves as an ideal gas in the 5M formulation, such that $p = nk_BT$, where k_B is the Boltzmann constant and T is temperature. The mean energy is calculated as $\epsilon = \frac{3}{2}k_BT + \frac{1}{2}m|\vec{u}|^2$. Assuming steady state and neglecting the inertial term in Eq. (4) recovers the drift-diffusion equation for electrons.

A. Electron source terms

In the electron continuity equation, the electron source term is only due to ionization, i.e., $\dot{n}_e = \dot{n}_{iz}$. To determine $\dot{n}_{iz}$, the ionization collision cross-section is calculated using the Drawin model,[15,16] as in Ref. 12,

$$Q(\epsilon) = 2.66\pi a_0^2 \left(\frac{\epsilon_{1\lambda}^H}{\epsilon_{1\lambda}} \right)^2 \xi_1 \beta_1 g(u), \tag{6}$$

where,

$$g(u) = \frac{u-1}{u^2} \ln(1.25\beta_2 u), \tag{7}$$

$u = \epsilon/\epsilon_{1\lambda}$, $\epsilon_{1\lambda}$ is the threshold ionization energy for the species of interest (here, xenon), $\epsilon_{1\lambda}^H$ is the ionization energy of hydrogen (13.6 eV), ξ_1 is the effective number of electrons in the outer shell (here, 6), a_0 is the Bohr radius, and $\beta_1 = \beta_2 = 1$ is used. In the present 5M model, this cross section is integrated over a Maxwellian energy distribution function to get the rate coefficient, k_{iz}, and the ionization source term is computed as $\dot{n}_{iz} = n_e n_n k_{iz}$.

The momentum exchange collisions for electrons are treated using a Krook operator,

$$\vec{C}_e = -n_e \sum_s \nu_{m,s}(\vec{u} - \vec{u}_s), \tag{8}$$

where $\nu_{m,s}$ is the momentum transfer collision frequency between electrons and species s. Because the plasma density is low and for consistency with the PIC-MCC model, electron-ion Coulomb collisions are neglected in this study. Thus, the net electron momentum exchange collision frequency is given by

$$\nu_e = \nu_{en} + \nu_{in} + \nu_a, \tag{9}$$

where the electron-neutral collision frequency is approximated as $\nu_{en} = 2.5 \times 10^{-13} n_n$, ν_{in} accounts for scattering due to inelastic collisions (e.g., ionization), and ν_a is the anomalous electron scattering frequency. A simple model for Bohm-like scaling of the anomalous electron scattering frequency is used, $\nu_a = \alpha_\nu \omega_{ce}$, where

$$\alpha_\nu = \begin{cases} \alpha_{\nu,0} & x < x_0, \\ \alpha_{\nu,0} + \frac{x - x_0}{x_1 - x_0}(\alpha_{\nu,1} - \alpha_{\nu,0}) & x_0 \le x < x_1, \\ \alpha_{\nu,1} & x_1 \le x. \end{cases} \tag{10}$$

Here, $\alpha_{\nu,0} = 0.01$, $\alpha_{\nu,1} = 0.25$, $x_0 = 0.0225$ m, $x_1 = 0.0275$ m, and $\omega_{ce} = eB/m_e$ is the electron cyclotron frequency. It should be noted that while this form of the anomalous electron scattering frequency is used for its simplicity to aid in this benchmarking activity, it is not representative of the spatial distribution inferred from experimental measurements (cf, Refs. 13, 17).

The energy source term due to inelastic collisions only includes a contribution from ionization, as excitation losses are neglected:

$$\mathcal{C} = -n_e \nu_{iz} \Delta\epsilon_{iz}, \tag{11}$$

where $\nu_{iz} = n_n k_{iz}$ is the ionization collision frequency and $\Delta\epsilon_{iz} = 12.1$ eV for xenon.

B. Ion source terms

In HETs ionization and acceleration simultaneously occur. This can yield two populations of ions, i.e., high-energy (beam-like) ions that are ionized in the ionization region where the potential is high and low-energy ions that are ionized in the acceleration region where the potential is low.[17,18] Including this effect may be important to capture the plume physics, particularly the broadening of the plume and the flow of ions towards the pole pieces. As such, a two-fluid approach is used for the ions, which are divided into high energy and low energy subpopulations. The macroscopic ion properties can then be calculated as the weighted sum of the contributions from the two subpopulations:

$$n_i = n_{i,he} + n_{i,le}, \tag{12}$$

$$n_i\vec{u}_i = n_{i,he}\vec{u}_{i,he} + n_{i,le}\vec{u}_{i,le}, \tag{13}$$

$$n_i\epsilon_i = n_{i,he}\epsilon_{i,he} + n_{i,le}\epsilon_{i,le}, \tag{14}$$

where the subscripts he and le refer to the high energy and low energy subpopulations, respectively.

The ion source terms in the continuity equations include both contributions from ionization and charge exchange (CEX) collisions. The reaction equations for the CEX collisions can be written as

$$\mathrm{Xe}^+_{\mathrm{he,fast}} + \mathrm{Xe}_{\mathrm{slow}} \rightarrow \alpha\mathrm{Xe}^+_{\mathrm{he,slow}} + (1-\alpha)\mathrm{Xe}^+_{\mathrm{le,slow}} + \mathrm{Xe}_{\mathrm{fast}}, \tag{15}$$

$$\mathrm{Xe}^+_{\mathrm{le,fast}} + \mathrm{Xe}_{\mathrm{slow}} \rightarrow \mathrm{Xe}^+_{\mathrm{le,slow}} + \mathrm{Xe}_{\mathrm{fast}}, \tag{16}$$

which leads to the following source terms for the continuity equations:

$$\dot{n}_{i,he} = \alpha\dot{n}_{iz} - (1-\alpha)\dot{n}_{CEX,he}, \tag{17}$$

$$\dot{n}_{i,le} = (1-\alpha)\dot{n}_{iz} + (1-\alpha)\dot{n}_{CEX,he}, \tag{18}$$

where $\dot{n}_{i,he} = n_{i,he}n_n\nu_{CEX,he}$ accounts for the total number of CEX ions lost from the high-energy population and the number of newly created slow ions which get distributed between the high energy and low energy populations is determined by α. Although the low energy ions undergo CEX collisions at a rate $\dot{n}_{i,le} = n_{i,le}n_n\nu_{CEX,le}$, the newly created slow ions are assumed to remain in the same subpopulation, which is why $\dot{n}_{i,le}$ does not show up in the source term of the continuity equation but does show up in the conservation of momentum and mean energy. The creation of charge exchange ions is included throughout the domain, in both the discharge channel and the plume. The parameter α determines the splitting of source terms in Eqs. (3)-(4) between the two ion subpopulations and is defined based on the local plasma potential as

$$\alpha = \begin{cases} \alpha_0 & \phi < \phi_{th,0}, \\ \alpha_0 + (\alpha_1 - \alpha_0)\frac{\phi - \phi_{th,0}}{\phi_{th,1} - \phi_{th,0}} & \phi_{th,0} \leq \phi \leq \phi_{th,1}, \\ \alpha_1 & \phi_{th,1} < \phi, \end{cases} \tag{19}$$

where $\alpha_0 = 0$, $\alpha_1 = 0.999$, $\phi_{th,0} = 30$ V, and $\phi_{th,1} = 60$ V are used here. The non-unity value of α_1 prevents full depletion of the low energy ion population in the upstream, high plasma potential region of the discharge channel, which aids in numerical stability. The ion-neutral charge exchange (CEX) collisions are included assuming that the ions are cold with a velocity much greater than the neutral velocity, such that the CEX collision frequency can be calculated as

$$\nu_{CEX,s} = n_n\sigma_{CEX,s}(\epsilon_i)\left\|\vec{u}_{i,s}\right\|, \tag{20}$$

where n_n is the neutral number density, $\sigma_{CEX,s}$ is the CEX cross-section and $\epsilon_{i,s}$ is the ion mean energy for $s = he, le$. Although true in the plume, as can be seen in Sec. VII, this assumption is violated in the upstream region of the discharge channel. Accordingly, the implementations of the CEX collisions is currently being reevaluated. The CEX cross-sections are obtained from Miller et al.[19]

In the ion momentum equations, the source terms for the subpopulations are

$$\vec{C}_{i,he} = \alpha\dot{n}_{iz}\vec{u}_n + \dot{n}_{CEX,he}(\alpha\vec{u}_n - \vec{u}_{i,he}), \tag{21}$$

$$\vec{C}_{i,le} = (1-\alpha)\left(\dot{n}_{iz} + \dot{n}_{CEX,he}\right)\vec{u}_n + \dot{n}_{CEX,le}\left(\vec{u}_n - \vec{u}_{i,le}\right), \tag{22}$$

where the Krook operator is again used for the ion-neutral collisions and $\vec{u}_n$ is the neutral bulk velocity. In the high energy ion drag term, $\alpha\dot{n}_{iz}$ is the momentum gained due to ionization, $\dot{n}_{CEX,he}\vec{u}_{i,he}$ is the momentum lost due to CEX collisions, $\alpha\dot{n}_{CEX,he}\vec{u}_n$ is the momentum gained due to the new slow ions. In the low energy ion drag term, $(1-\alpha)\dot{n}_{iz}\vec{u}_n$ is the momentum gained due to ionization, $(1-\alpha)\dot{n}_{CEX,he}\vec{u}_n$ is the momentum gained due to ions produced in the CEX collisions between the high energy ions and neutrals, $\dot{n}_{CEX,le}\vec{u}_n$ is the momentum gained due to ions produced in the CEX collisions between the low energy ions and neutrals, and $\dot{n}_{CEX,le}\vec{u}_{i,le}$ is the momentum lost due to CEX collisions between the low energy ions and neutrals.

Lastly, in the ion energy equations, the source terms are

$$\mathcal{C}_{i,he} = \alpha\epsilon_n\dot{n}_{iz} + \dot{n}_{CEX,he}(\alpha\epsilon_n - \epsilon_{i,he}), \tag{23}$$

$$\mathcal{C}_{i,le} = (1-\alpha)\epsilon_n\left(\dot{n}_{iz} + \dot{n}_{CEX,he}\right) + \dot{n}_{CEX,le}\left(\epsilon_n - \epsilon_{i,le}\right), \tag{24}$$

where ϵ_n is the neutral mean energy. In the high energy ion loss term, $\alpha\epsilon_n\dot{n}_{iz}$ is the energy gained due to ionization, $\dot{n}_{CEX,he}\alpha\epsilon_n$ is the energy gained due to the creation of new slow ions, and $\dot{n}_{CEX,he}\epsilon_{i,he}$ is the energy lost due to CEX collisions. In the low energy ion loss term, $(1-\alpha)\dot{n}_{iz}\epsilon_n$ is the energy gained due to ionization, $(1-\alpha)\dot{n}_{CEX,he}\epsilon_n$ is the energy gained due to ions produced in the CEX collisions between the high energy ions and neutrals, $\dot{n}_{CEX,le}\epsilon_n$ is the energy gained due to ions produced in the CEX collisions between the low energy ions and neutrals, and $\dot{n}_{CEX,le}\epsilon_{i,le}$ is the energy lost due to CEX collisions between the low energy ions and neutrals.

C. Conductive heat flux

As has been done in many fluid electron models for HETs,[2,5] although notably not all,[3] we assume $\vec{q}$ to follow Fourier's law for electrons,

$$\vec{q}_e = -\bar{\bar{\kappa}}_e\nabla T_e, \tag{25}$$

where $\bar{\bar{\kappa}}_e$ is the electron thermal conductivity tensor defined in 2D relative to the magnetic field lines as,

$$\bar{\bar{\kappa}}_e = \begin{bmatrix} \kappa_{e\parallel} & 0 \\ 0 & \kappa_{e\perp} \end{bmatrix}. \tag{26}$$

The field-aligned and cross-field electron thermal conductivities for a partially-ionized plasma are given as,[16]

$$\kappa_{e\parallel} = \frac{2.4}{1 + \nu_{ei}/\left(\sqrt{2}\nu_e\right)}\frac{nk_B^2T_e}{m_e\nu_e}, \tag{27}$$

$$\kappa_{e\perp} = \frac{1}{1+\Omega_H^2}\kappa_{\parallel}, \tag{28}$$

where $\Omega_H = ...$ Here, we assume that the electron-ion Coulomb collision frequency $\nu_{ei} = 0$. The validity of using Fourier's law for the heat flux will be discussed in Sec. VII.

The conductive heat flux is neglected in the ion energy equations, i.e., $\vec{q}_i = 0$.

D. Boundary conditions

A significant source of complexity in simulating HETs is the diverse set of boundary conditions. Separate consideration must be given to inflow and outflow boundaries, dielectric materials (including those with secondary electron emission), conducting materials, and particle emission sources (e.g., neutral injection and cathode emission surfaces), shown in Fig. 1. Unlike quasineutral models which typically use one-dimensional sheath theory to determine the electron boundary conditions at material interfaces, the 5M model can self-consistently utilize the electron properties at material interfaces to compute the fluxes. This is both a benefit and source of difficulty which requires careful treatment.

1. Energy-limited kinetic fluxes

A common wall boundary condition in fluid modeling for low temperature plasmas is to use the one-sided thermal fluxes of a stationary Maxwellian distribution. However, such an approach neglects the potential deceleration of incoming electrons which can occur next to boundaries in the presence of a strong electric field. This picture becomes increasingly complex when considering a secondary electron emission from dielectric surfaces, as the sheath can vary from classical (electron repelling) to space charge limited (SCL) to inverse (electron attracting).[20,21] In the SCL to inverse sheath transition, a virtual cathode can form over length scales much smaller than the Debye length, which can be difficult to resolve in both kinetic and fluid simulations. In these regimes, the trapping of secondary electron must also be captured. We have observed that insufficient resolution of the sheath can lead to numerical fluctuations and even unstable simulations. To account for the effect of the boundary electric field on primary electrons, we consider truncating the particle VDFs at some threshold velocity $v_0 > 0$, such that particles with velocities $0 < v < v_0$ will be reflected. Assuming a lower bound of $v_0 = \sqrt{\frac{2e\phi_b}{m_e}}$, where $\phi_b = E_b \Delta x$ is the effective potential associated with boundary electric field, E_b, the one-sided (+) fluxes for quantity Q in the x direction can be calculated by taking moments of Eq. (2) as

$$\Gamma_Q^+ = \int_{v_0}^{\infty}\int_{-\infty}^{\infty}\int_{-\infty}^{\infty} Q v_x f_M(\vec{v}) d^3\vec{v} \tag{29}$$

for $Q = \{n, n\vec{v}, \frac{1}{2}nm|\vec{v}|^2\}$, which we will refer to as the energy-limited kinetic flux (ELKF). The $(-)$ fluxes can be calculated analogously by considering integral bounds from $-\infty$ to v_0. Considering both the (+) and $(-)$ fluxes,

$$\Gamma_n^{\pm} = \pm\frac{1}{4}n\sqrt{\frac{8k_BT}{\pi m}}\left[\exp\left(-\tilde{u}_{0x}^2\right) + \sqrt{\pi}\tilde{u}_x\left\{-\mathrm{erf}\left(\tilde{u}_{0x}\right) \pm 1\right\}\right], \tag{30}$$

$$\Gamma_{nu_x}^{\pm} = \pm\frac{nk_BT}{m}\left[\frac{\tilde{u}_0 + \tilde{u}_x}{\sqrt{\pi}}\exp\left(-\tilde{u}_{0x}^2\right) + \left(\frac{1}{2} + \tilde{u}_x^2\right)\left\{-\mathrm{erf}\left(\tilde{u}_{0x}\right) \pm 1\right\}\right], \tag{31}$$

$$\Gamma_{nu_y}^{\pm} = \Gamma_n^{\pm}u_y, \tag{32}$$

$$\Gamma_{nu_z}^{\pm} = \Gamma_n^{\pm}u_z, \tag{33}$$

$$\begin{aligned}\Gamma_{n\epsilon}^{\pm} = \pm\frac{1}{4}nk_BT\sqrt{\frac{8k_BT}{\pi m}}\Bigg[&\left(2 + 3\tilde{u}_x\tilde{u}_0 + \tilde{u}_{0x}^2 + \tilde{u}_y^2 + \tilde{u}_z^2\right)\exp\left(-\tilde{u}_{0x}^2\right) \\ &+ \left(\frac{5}{2} + \tilde{u}_x^2 + \tilde{u}_y^2 + \tilde{u}_z^2\right)\sqrt{\pi}\tilde{u}_x\left\{-\mathrm{erf}\left(\tilde{u}_{0x}\right) \pm 1\right\}\Bigg],\end{aligned} \tag{34}$$

giving the mass, momentum, and energy fluxes, respectively, where $\tilde{u}_j = u_j/u_m$, $\tilde{u}_0 = u_0/u_m$, and $\tilde{u}_{0j} = (v_0 - u_j)/u_m$ for $j = x, y, z$, and $u_m = (2k_BT/m)^{1/2}$ is the most probable speed.

The ELKF approach has the key benefit of allowing the fluxes to exactly match those of a truncated Maxwellian VDF, which is more physically consistent with expectations from kinetic theory at plasma-material interfaces.[22] The limiting case considering $v_0 = 0$ m/s has been used in previous works.[5] However, in the presence of a large electric field such as can occur at the sheath-wall interface (e.g., at the surface of a dielectric with significant charge accumulation), the lower bound of Eq. (29) can no longer be taken to be zero.

2. *Conducting wall*

Conducting walls are treated as absorbing boundaries with fixed plasma potential. Ghost cells utilize a zero Dirichlet condition for density and pressure and a Neumann condition for all three components of velocity.

3. *Dielectric wall*

Secondary electron emission is included at dielectric boundaries. Only true secondary emission is considered, i.e., no reflection of electrons off boundaries. A simple linear model is used for the secondary electron emission coefficient,

$$\delta_{SEE} = \frac{\epsilon_{e,im}}{\epsilon^*}, \tag{35}$$

where the electron impact energy is computed as

$$\epsilon_{e,im} = \frac{\Gamma_{n\epsilon,e}}{\Gamma_{n,e}}, \tag{36}$$

using fluxes computed with the ELKF method. Here, in accordance with past studies of SPT-100-like thrusters with boron nitride walls, a value of $\epsilon^* = 51.1$ eV is used.[12]

The surface charge density collected at a dielectric boundary is

$$\sigma(t) = e\int_0^t \left(\Gamma_{i,he} + \Gamma_{i,le} - \Gamma_{pe} + \Gamma_{se}\right) dt, \tag{37}$$

where Γ_i is the incoming ion flux, the subscripts he and le denote the high energy and low energy subpopulations, respectively, Γ_{pe} is the incoming (primary) electron flux, and Γ_{se} is the outgoing (secondary) electron flux. The surface charge is accumulated from a charge-free initial condition at the start of the simulation. At steady state, σ should be constant and the ion and electron net currents should balance, i.e., $\Gamma_{i,he} + \Gamma_{i,le} = \Gamma_{pe} - \Gamma_{se}$.

4. Uniform cathode continuity injection

For steady-state, DC operation in the absence of leakage current (e.g., caused by electron or ion fluxes to vacuum chamber walls or thruster body) the anode and cathode currents in a HET should be equal. As such, a simple cathode model is simply to inject electrons at the cathode boundary such that $I_c = I_a$, where I_c and I_a are the net currents to the cathode and anode surfaces, respectively. In this work we assume a nearly uniform emission of electrons over the entire cathode boundary using the ELKF with a fixed electron emission temperature of $T_{e,cat} = 3$ eV.

The small deviation from uniform emission is due to the redistribution of electron current from the ELKF. In regions with inverse sheaths adjacent to the cathode boundary, the ELKF boundary condition will limit the output of electrons to account for local trapping. To maintain current continuity between the anode and cathode, the net emitted fluxes at each boundary cell are rescaled by I_a/I_{emit}, where I_{emit} is the limited current after considering trapping but before rescaling for current continuity.

E. Numerical methods

The mass and momentum equations for electrons, as well as the mass, momentum, and energy equations for both ion subpopulations, are solved in a coupled manner using a second-order strong stability preserving Runge-Kutta (SSP-RK2) method.[23] Because of the severe timestep restriction imposed by the large field-aligned thermal conductivity, the electron energy equation is solved in a semi-implicit decoupled manner, with the mean energy ϵ_e assumed constant throughout the RK substeps. Using the relationship between mean energy, internal energy, and kinetic energy, we can rewrite $\vec{q}_e$ from Eq. (25) as,

$$\vec{q}_e = -\frac{2}{3k_B}\bar{\bar{\kappa}}_e \nabla\left(\epsilon_e - \frac{1}{2}m_e \left\|\vec{u}_e\right\|^2\right). \tag{38}$$

The primitive electron energy equation can then be written as

$$\begin{aligned}\frac{\partial \epsilon_e}{\partial t} + \frac{1}{n_e}\left[\nabla\cdot\left(n_e\epsilon_e\vec{u}_e + \bar{\bar{p}}_e\cdot\vec{u}_e\right) - \epsilon_e\nabla\cdot\left(n_e\vec{u}_e\right) - \frac{2}{3k_B}\nabla\cdot\left(\bar{\bar{\kappa}}_e\nabla\epsilon_e\right) + \frac{m_e}{3k_B}\nabla\cdot\left(\bar{\bar{\kappa}}_e\nabla\left\|\vec{u}_e\right\|^2\right)\right] \\ = -\frac{1}{n_e}\left[en_e\vec{u}_e\cdot\vec{E} + \dot{n}_{iz} - \mathcal{C}\right],\end{aligned} \tag{39}$$

where the diffusion of the mean energy and kinetic energy have been separated. Equation (39) is discretized and solved semi-implicitly using a generalized θ method,

$$\epsilon_e^{k+1} = \epsilon_e^k + \theta\Delta t F(U^k) + (1-\theta)\Delta t G(U^{k+1}), \tag{40}$$

where θ is the weighting coefficient between the explicit and implicit treatment, $F(U)$ is the implicit update operator, $G(U)$ is the explicit update operator, and U^k represents the vector of state variables at the k-th iteration. Here, we treat only the diffusion of the mean energy implicitly, i.e., $F(U) = \frac{2}{3k_B}\nabla\cdot\left(\bar{\bar{\kappa}}_e\nabla\epsilon_e\right)$, consistent with the treatment of the energy equation in previous studies.[2] A value of $\theta = 0.5$, as is used here, corresponds to Crank-Nicolson, a value of $\theta = 0$ corresponds to forward Euler, and a value of $\theta = 1$ corresponds to backwards Euler. Adaptive time-stepping based on the CFL condition is used to ensure stability throughout the simulation. The average timestep for the simulation is $\Delta t \approx 8$ ps.

Second-order spatial reconstruction of the primitive variables is performed using the Monotonic Upwind Scheme for Conservation Laws (MUSCL) with a Van Leer flux limiter on a structured, uniform grid with $\Delta x = \Delta y = 0.1$ mm.[24] A Steger-Warming (SW) flux vector splitting scheme is used with an entropy fix to prevent spurious oscillations about sonic points.[25] The ELKF method described in the previous section is used to compute the fluxes at all boundaries.

The simulation is initialized with uniform electron and ion number densities of $n_0 = 4.0 \times 10^{17}$ m^{-3}. The ion number density is split is $n_{0,he} = 3.9 \times 10^{-17}$ m^{-3} and $n_{0,le} = 0.1 \times 10^{17}$ m^{-3} for the high energy and low energy populations, respectively. The initial electron temperature is a uniform $T_{e0} = 10$ eV and the initial ion temperatures are both $T_{i0} = 0.5$ eV.

IV. The particle-in-cell Monte Carlo collision model

In the particle-in-cell (PIC) method, Eq. (2) is solved by discretizing the phase space with individual macroparticles representing a collection of physical particles of a given species. The number of physical particles a single macroparticle represents is given by the particle weight w_p. The equations of motion for each macroparticle of species s (electrons or singly-charged xenon ions) are given as

$$\frac{\partial \vec{v}_p}{\partial t} = -\frac{q_s}{m_s}\left(\vec{E} + \vec{v}_p \times \vec{B}\right), \tag{41}$$

$$\frac{\partial \vec{x}_p}{\partial t} = \vec{v}_p, \tag{42}$$

where $\vec{x}_p$ and $\vec{v}_p$ are the position in physical space and in velocity space of macroparticle p, respectively. The unknowns $\vec{x}_p$ and $\vec{v}_p$ are evolved on a staggered grid in time using the Boris push method with a timestep of 10 ps.[26] The computational domain of the problem is split into a structured grid with a uniform cell size of $\Delta x = \Delta y = 0.2$ mm in each dimension.

The cloud-in-cell (CIC) scheme, i.e., linear interpolation between a macroparticle and its surrounding cell centers, is used.[27] Moments of Eq. (2) may be calculated based on the particle population by summing the contributions from each particle.

A. Initial conditions

The model is initialized with uniform electron and ion densities of 4×10^{17} m^{-3} at 20 macroparticles per cell per species, yielding a macroparticle weight of 2.136×10^8 true particles per macroparticle. Electrons are initialized with a stationary Maxwellian VDF at a temperature of $T_{e,init} = 10$ eV, while ions are initialized with a drifting Maxwellian VDF at a temperature of $T_{i,init} = 0.5$ eV and an initial downstream axial mean velocity of $u_{i,init} = 5$ km/s. All boundary quantities that are accumulated in time (e.g. surface charge on dielectric boundaries) are initialized to zero.

B. Boundary conditions

1. *Conducting wall*

Both the anode and cathode boundaries are treated as absorbing walls, meaning that any particles crossing through these boundary surfaces are removed from the simulation and counted towards the net currents through their respective surface. No particles are injected at the anode boundary. In order to enforce current continuity between the anode and cathode, i.e., $I_c = I_a$, electron macroparticles are injected uniformly through the cathode boundary based on the computed anode and cathode (pre-injection) currents at any given time. The electrons injected at the cathode boundary are drawn from a stationary Maxwellian VDF at a temperature of $T_{e,cat} = 3$ eV.

2. *Dielectric wall*

Dielectric walls are also modeled as absorbing boundaries where any electron or ion impacting the wall is removed from the simulation and counted towards the current to the wall. The initial surface charge density of dielectric surfaces is set to zero. The surface charge and current are computed by tracking the net flux of charges through the dielectric boundary. In this process, no spatial weighing function is applied, meaning that the impact of a charge onto the dielectric boundary is applied in full to only the cell interface within which it impacted the wall. Furthermore, electron impacts on the dielectric boundaries may produce secondary electrons that are initialized based on a Maxwellian flux distribution at a temperature $T_{e,SEE} = 2$ eV. The SEE yield is given by Eq. (35), where for the PIC-MCC model, $\epsilon_{e,im} = \frac{1}{2} m_e \|\vec{v}_e\|^2$. In order to account for fractional yield without varying macroparticle weight, an additional secondary electron is injected using the fractional part of the SEE yield as the probability of injection.

C. Collisions

Elastic momentum exchange collisions and ionization collisions between electrons and the neutral background population are modeled using the Monte Carlo Collisions (MCC) algorithm with the Null-Collision method.[28] The neutral transport model described in (50) is employed to compute the neutral density $n_n(x)$. Collision cross-sections are taken to be identical to those used in the fluid model.

1. *Ionization collisions*

Ionization cross-sections are obtained from the Drawin model, given in Eq. (6). An ionization collision event between a (primary) electron and the neutral background leads to the injection of a (secondary) electron and an ion at the same location as the collision event. The pre-collision energy for electron-neutral collisions is given as

$$\epsilon_{pre} = \frac{1}{2} m_e \|\vec{g}\|^2 \approx \frac{1}{2} m_e \|\vec{v}_{e,pre}\|^2, \tag{43}$$

where $\vec{g}$ is the relative velocity between the primary electron and the neutral background, and $\vec{v}_{e,pre}$ is the pre-collision velocity of the primary electron. The post-collisional energy for an ionization event ϵ_{post} can be expressed as

$$\epsilon_{post} = \epsilon_{pre} - \Delta\epsilon_{iz}. \tag{44}$$

Due to the large difference in electron and ion masses, the generated ion can be assumed to have a post collision velocity, $\vec{v}_i$, equal to that of the neutral background population, $\vec{u}_n$. Both the primary and secondary electrons are isotropically scattered, and the post-collisional energy is assumed to be split in random proportions between the primary and secondary electrons. The post-collision velocities of the primary and secondary electron are then randomly selected with uniform probability.

2. *Momentum-transfer collisions*

The momentum-transfer collision frequency for electrons includes both electron-neutral elastic scattering and an anomalous electron scattering frequency, given by Eq. (10). When a momentum-transfer collision occurs, the electron is scattered isotropically. In the laboratory frame, the scattered electron experiences a slight energy loss such that the pre- to post-collision energy fraction is given by

$$\frac{\epsilon_{post}}{\epsilon_{pre}} = 1 - \frac{2m_e}{m_n}\left(1 - \cos\theta\right), \tag{45}$$

where m_n is the neutral atom mass and θ is the scattering angle. The post-collision electron velocity is then given by

$$v_{e,post} = v_{e,pre}\sqrt{1 - \frac{2m_e}{m_n}(1 - \cos\theta)}; \tag{46}$$

3. *Charge-exchange collisions*

Charge-exchange collisions are included in the model and act as a drag and scattering mechanism for ions, which exchange their charge with background neutrals. The effect on the neutral background is neglected as with all other collisions within the MCC algorithm. In contrast to electron-neutral collisions, the neutral is taken into account for the relative velocity as neutral and ion velocities can be comparable. The collision energy is given as

$$\epsilon_{pre} = \frac{1}{2} m_i \|\vec{g}\|^2 = \frac{1}{2} m_i \|\vec{v}_i - \vec{v}_n\|^2, \tag{47}$$

where $\vec{v}_i$ is the ion macroparticle velocity and $\vec{v}_n$ is the neutral velocity, which has been sampled from a drifting Maxwellian with $\vec{u}_n$ from the fixed neutral velocity profile and a temperature of 0.5 eV. The velocity of the ion macroparticle undergoing the collision is interchanged with that of the sampled neutral, $\vec{v}_n$.

V. Poisson's equation

Making use of the electrostatic assumption, Poisson's equation is solved for the plasma potential,

$$\nabla^2\phi = -\frac{e(Zn_i - n_e)}{\epsilon_0'}, \tag{48}$$

where ϕ is the plasma potential and Z is the average charge state of the ions. Because only singly-charged ions are considered in this work, $Z = 1$. The electric field is then calculated as $\vec{E} = -\nabla\phi$. Poisson's equation is solved in the same manner for both the 5M and PIC-MCC methods, with plasma potential calculated at cell centers and electric fields calculated at cell interfaces. For the interpolation scheme used in the PIC-MCC implementation, the cell interface electric fields are averaged into the grid nodes for linear interpolation back to particles, whereas the 5M implementation averages neighboring field values to the cell center. Second-order central differencing is used for both models.

A. Boundary Conditions

The boundary conditions for Poisson's equation vary depending on the type of interface. Along the anode and cathode boundaries, Dirichlet conditions of $\phi_a = 300$ V and $\phi_c = 0$ V are applied, respectively. Along the dielectric channel walls and pole pieces, a Neumann condition is imposed based on the surface charge, such that

$$\vec{E}_w = \frac{\sigma}{\epsilon_0'}\hat{e}_n, \tag{49}$$

where $\hat{e}_n$ is the surface normal vector pointing away from the wall.

B. Numerical Methods

Equation (48) is solved using the HYPRE library with a PFMG preconditioner and GMRES solver for both the 5M and the PIC-MCC models.[29]

VI. Neutral transport model

Hall effect thrusters are dynamic systems which exhibit a wide range of timescales from kHz to GHz. Perhaps the most prominent oscillation is the breathing mode, which is characterized by a predator-prey type relationship between the ions and neutrals, has large amplitude, and is typically on the order of 10-30 kHz.[1] To allow for convergence of the system to steady state, a strategy used in previous kinetic simulations has been to use a simplified 1D transport law for neutrals,[12,14] based on particle conservation of the injected gas throughout the channel,

$$n_n(x) = n_{inj} - \frac{\dot{m}_{i,x}(x)}{m_i A u_{n,x}} \tag{50}$$

where the injected neutral density is $n_{inj} = \dot{m}_{inj}/A m_i u_{n,x}$, the axial neutral bulk velocity $u_{n,x}$ is assumed to be constant throughout the discharge channel, the channel area is $A = \pi\left(r_{out}^2 - r_{in}^2\right)$, r_{out} and r_{in} are the outer and inner radii, respectively, and the axial ion mass flow rate is calculated as

$$\dot{m}_{i,x}(x) = \frac{2}{r_{out} - r_{in}} \int_{r_{in}}^{r_{out}} m_i \Gamma_{i,x}(x,y)dy, \tag{51}$$

where $\Gamma_{i,x}(x,y)$ is the axial ion number density flux as a function of position. Here, a mass flow rate of 5 mg/s is used with a neutral velocity of $u_{n,x} = 270$ m/s in the discharge channel. Because the cross-sectional area changes discontinuously at the channel exit, a different model must be used for the plume. In Ref. 12, the neutral density in the plume is assumed to be constant. In reality, a significant variation in neutral density is expected in the near-field plume, particularly in the radial direction.[30] Here, to approximate a

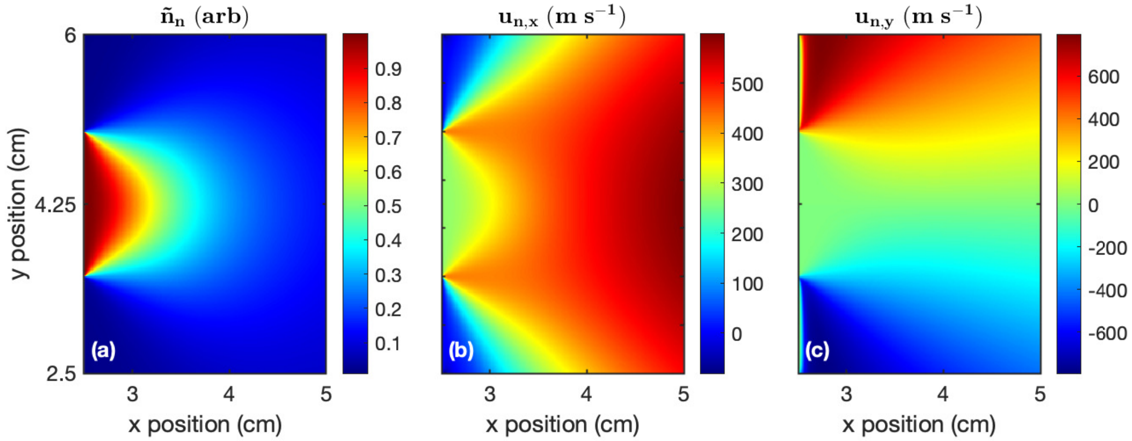

Figure 2. Contour plots of the (a) normalized neutral density, (b) neutral axial bulk velocity, and (c) neutral radial bulk velocity in the plume.

more realistic neutral density profile, a single standalone fluid simulation of the plume is conducted assuming known plume inlet conditions (i.e., channel exit conditions) and is run to steady state. The resulting density distribution is normalized and rescaled at each time step to form a continuous density profile with that of the simplified neutral law given by Eq. (50). The neutral velocity throughout the domain is assumed to be constant. The normalized density profile, axial velocity profile, and radial velocity profile in the plume are shown in Fig. 2(a)-(c), respectively.

VII. Results: Model comparison

Both the 5M and PIC-MCC models are run for 50 μs, at which point the they are at steady state. The 5M quantities shown in this section are instantaneous results at $t = 50$ μs, whereas the PIC-MCC quantities are averaged between $t = 30$ μs and $t = 50$ μs using samples taken every 1 ns. The steady state discharge currents are 10.1 A and 14.7 A for the 5M and PIC-MCC models, respectively.

Selected two-dimensional contours of the steady state plasma properties are shown in Fig. 3, with the left column showing 5M results and the right column showing the PIC-MCC results. Figures 3(a) and (b) show the ion density, Figs. 3(c) and (d) show the electron density, Figs. 3(e) and (f) show the electron temperature, and Figs. 3(g) and (h) show the plasma potential. The 2D contour plots are accompanied by centerline slices in Fig. 4. Figures 4(a)-(h) show the electron and ion densities, neutral number density, plasma potential, axial electric field, electron temperature, axial ion bulk velocity, axial electron bulk velocity, and azimuthal electron bulk velocity, respectively. For the PIC-MCC results, the electron temperature is computed as the isotropic temperature: $T_e = (T_{e,xx} + T_{e,yy} + T_{e,zz})/3$.

Comparing the ion densities in Figs. 3(a) and (b), and examining Fig. 4(a), several differences between the 5M and PIC-MCC results can be observed. First, the peak plasma density in the PIC-MCC result is higher than that of the 5M result by approximately 20% and is located at $x = 1.1$ cm rather than $x = 0.8$ cm. Simultaneously, the near-anode ion density in the 5M results is higher than that of the PIC-MCC result. These effects can be explained in part by the increased neutral density near the anode, shown in Fig. 4(b), which is a consequence of the larger ion recombination rate at the anode, as indicated by the increased ion backflow in Fig. 4(c). An additional contributing factor is the larger electron temperature in the upstream portion of the discharge channel in the 5M model, as the ionization rate coefficient increases rapidly at low T_e. It can also be seen that the ion density in front of the pole pieces is smaller in the 5M results than in the PIC-MCC results. This may be due to the combined effects of the Maxwellian assumption for each of the ion subpopulations and an under-prediction of the ion temperature, which can enhance radial diffusion of the ion beam. Finally, the increase in ion density in the near-field plume is smaller for the 5M model than the PIC-MCC model. This is a consequence of the increased maximum electron energy in the PIC-MCC result, which leads to increased ionization downstream. The local maximum density of this density bump coincides with $x = 2.75$ cm in the 5M model, where the anomalous scattering frequency profile saturates.

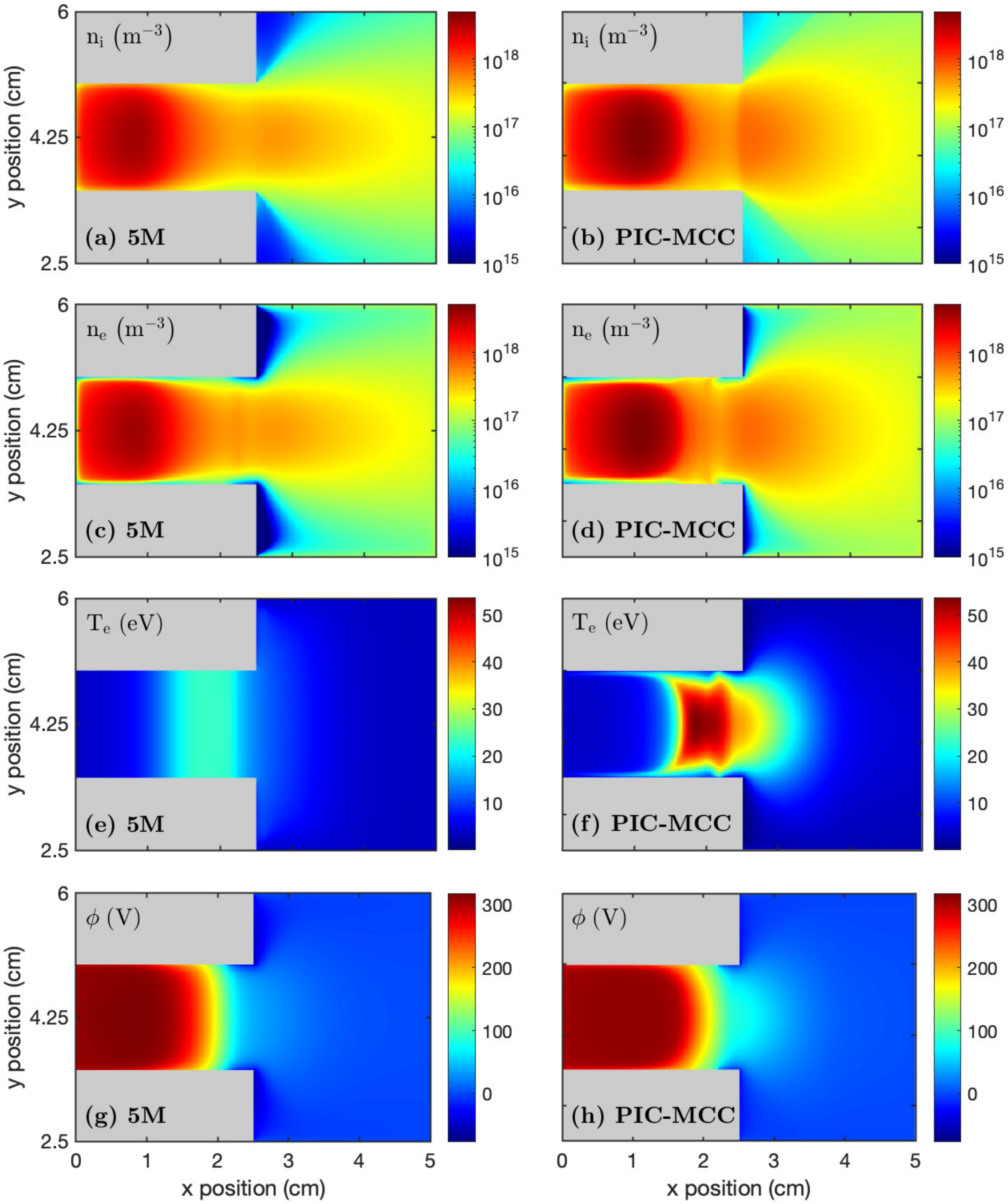

Figure 3. Two-dimensional contour plots of selected plasma properties from the 5M and PIC-MCC results.

This secondary population of ions produced at low plasma potential is also responsible for the decrease in axial ion bulk velocity seen in Fig. 4(c).

The electron density contours in Figs. 3(c) and (d) show similar qualitative trends to those of the ion density, but reveal additional interesting dynamics in the discharge channel around $x = 2.0$ cm, coinciding with the location where the anomalous electron scattering frequency begins to increase. In Fig. 3(d), and to a lesser extent in Fig. 3(c), it can be seen that the electron density remains high near the wall between $x = 1.7$ cm and $x = 2.2$ cm. In the PIC-MCC result at around $x = 2.1$ cm, the channel wall charges slightly positively, a space charge limited (SCL) inverse sheath develops, and an increase in density adjacent to the wall develops due to the trapped secondary electrons. In contrast, the 5M result shows a shallower decay in electron density towards the wall as compared to regions upstream or downstream in the discharge channel,

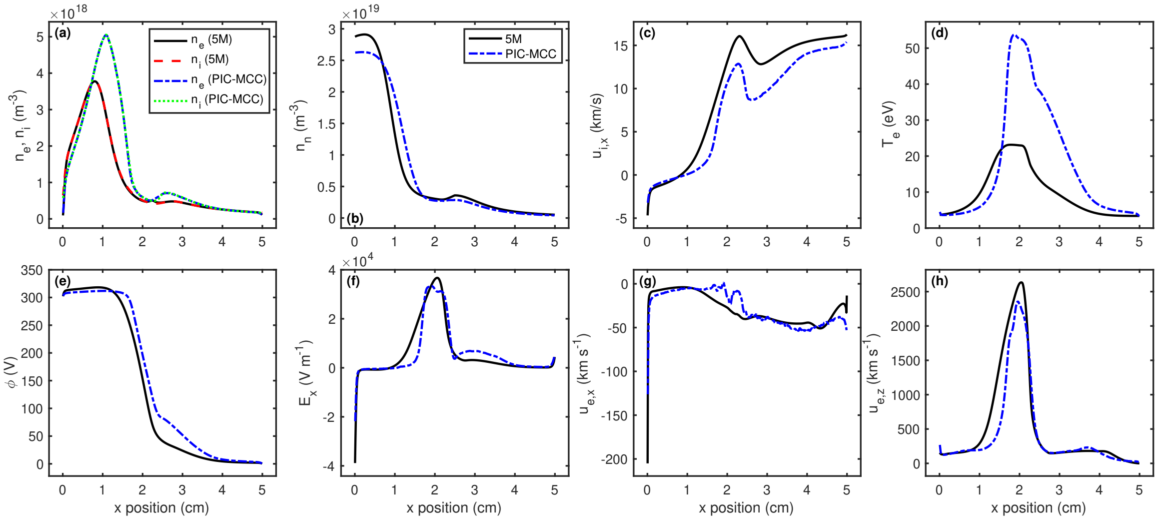

Figure 4. Selected plasma profiles comparing the fluid (solid/dash) and PIC-MCC (dotted/dot-dash) results along the discharge channel centerline.

but to a much lesser extent than the PIC-MCC result, and does not exhibit an inverse sheath. In the 5M result, the secondary electrons immediately thermalize with the bulk electron population, which prevents an SCL sheath from forming until an SEE coefficient of approximately 1.0.[31] Previous results have shown that at a wall with SEE, the VDF should look like the superposition of a truncated Maxwellian and a cold beam, which is a significant deviation from the assumptions of the 5M model.[22] A possible solution is to separate secondary electrons from different boundaries into separate populations, as has been done with the high and low energy ions.

The mean electron temperature for the 5M and PIC-MCC models are compared in Figs. 3(e) and (f) and Fig. 4(d). It is immediately evident that the maximum electron temperature predicted by the 5M model is much lower than that of the PIC-MCC result, by roughly a factor of 2.5. Furthermore, in contrast to the 5M result which shows isothermal magnetic field lines, the PIC-MCC results shows significant non-isothermality, consistent with several recent experimental studies.[32,33] The isothermality of the 5M field lines suggests that the model may over-predict the field-aligned heat flux or under-predict the cross-field heat flux as compared to the kinetic solution. This implies that the Fourier law used for electrons in Eq. (5) is insufficient to describe the observed electron heat flux in the kinetic result, as has been observed in other numerical studies using kinetic simulations.[12,34] The PIC-MCC results also show significant cooling of electrons immediately in front of the pole pieces. In this region, the electrons are still strongly magnetized due to the radial magnetic field and may be absorbed by the wall as they collide during their gyration. Accordingly, it has shown that the electron VDF becomes increasing non-Maxwellian as the magnetic field line angle of incidence to the wall increases towards 90°.[35] Combined with the SEE from dielectric surface, the electron VDF is likely highly non-Maxwellian in this region and deviations between the 5M and PIC-MCC results are to be expected.

Lastly, Figs. 3(g) and (h) and Fig. 4(e) compare the 5M and PIC-MCC plasma potentials. The 5M result has a peak plasma potential of 318 V at around $x = 0.9$ cm, whereas the PIC-MCC result has a peak of 312 V at $x = 1.0$ cm. As can be seen from Figs. 4(e) and 4(f), the increase in anode sheath potential is accompanied by a roughly two times larger electric field at the anode. The acceleration region, defined by the steep drop in plasma potential, is shifted downstream by 0.2 cm. The PIC-MCC result also has a change in slope of the potential gradient, i.e., change in axial electric field, beginning at around 75 V, rather than 40 V, which leads to the bump visible in the axial electric field shown in Fig. 4(f).

Figure 5 compares the current density profiles between the 5M and PIC-MCC models. The 5M results are shown in the left column and the PIC-MCC results are in the right column. Figures 5(a) and (b) show the planar (x-y) ion current densities $j_{i,p} = \sqrt{j_{i,x}^2 + j_{i,y}^2}$, Figs. 5(c) and (d) show the planar (x-y) electron current densities $j_{e,p} = \sqrt{j_{e,x}^2 + j_{e,y}^2}$, and Figs. 5(e) and (f) show the azimuthal electron current density.

Comparing Figs. 5(a) and (b), the profiles of the ion current densities are qualitatively similar, as are the maximum current densities. However, the 5M model over-predicts the ion current density near the anode,

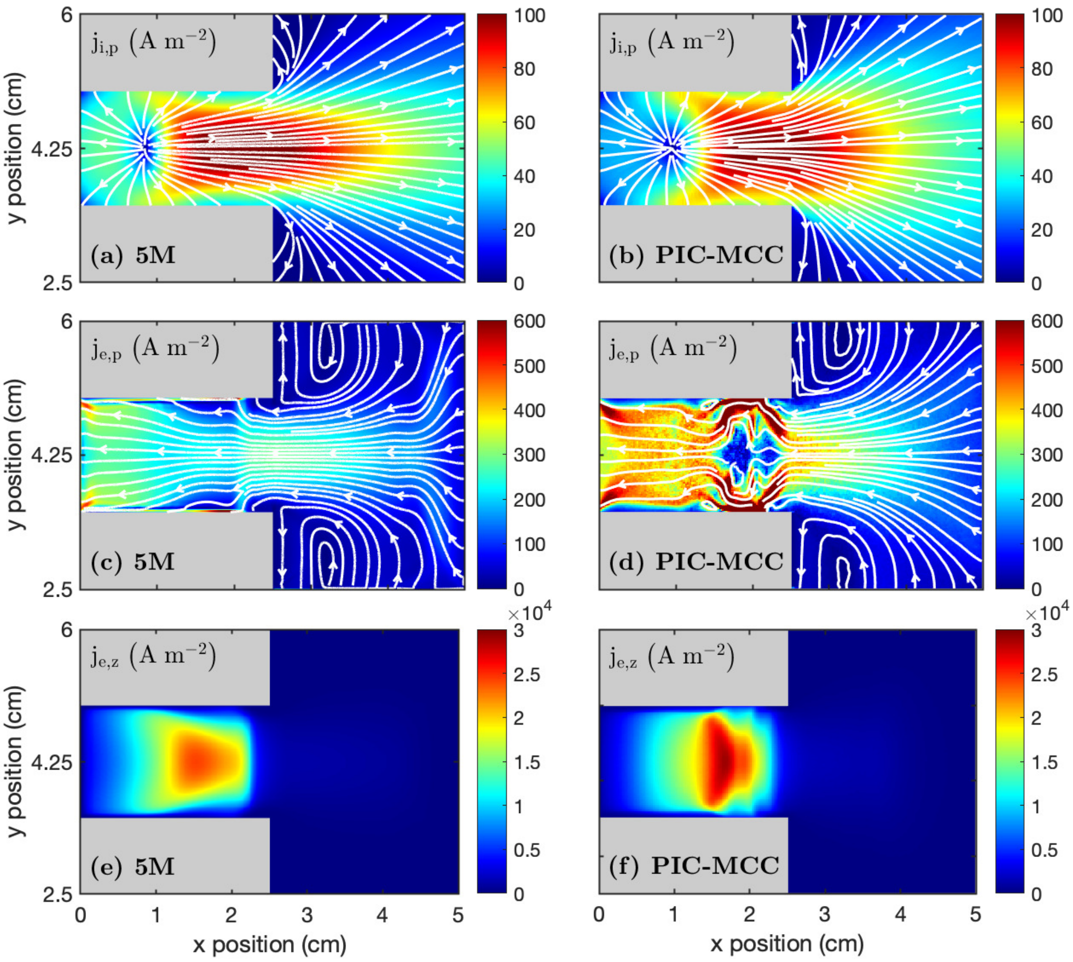

Figure 5. Two-dimensional contour plots and streamlines of the planar (axial-radial) ion current densities, planar electron current densities, and the azimuthal electron current densities from the 5M and PIC-MCC simulations.

the high current region is concentrated towards the center of the channel rather than extending radially towards the walls, and the divergence in the plume is reduced compared to the PIC-MCC results. The ion current density in the plume, particularly the decrease in current density towards the downstream extent of the domain and the flow of ions towards the pole pieces, depend strongly on the choice of α in Eq. (19).

Comparing Figs. 5(c) and (d), good qualitative agreement can be seen upstream of $x = 1.2$ cm and throughout the plume, but there are significant difference in the downstream portion of the discharge channel and the current density from the PIC-MCC simulation is generally larger than that of the 5M model. As can be seen in Fig. 4(g), the axial electron velocity approaches 0 m/s in this downstream region in the PIC-MCC results but not in the 5M results. In Ref. 12, this decrease in centerline electron current density and the observed branching structure are caused by the $\partial p_{yz}/\partial y$ pressure gradient cross-term in the azimuthal electron momentum equation, which is absent in the 5M model due to the isotropic pressure assumption. As such, a 10-moment (or higher order) fluid model which accounts for the anisotropic electron pressure tensor may be able to capture this effect. However, the high current density structures near the corners between the anode and channel walls include significant contributions from the inertial terms in the azimuthal momentum equation and therefore can be captured in the 5M model but not with the drift-diffusion approximation. It can also be seen that the 5M model features a significant electron current density through the sheath adjacent to the channel walls towards the anode, which is not seen in the PIC-MCC results.

Comparing Figs. 5(e) and (f), we again observe the strongest deviation between the 5M and PIC-MCC results in the downstream region of the discharge channel, where the anisotropic pressure effects may be non-negligible. By comparing Figs. 5(e) and (f) with Fig. 4(h), we can see that the deviation in azimuthal

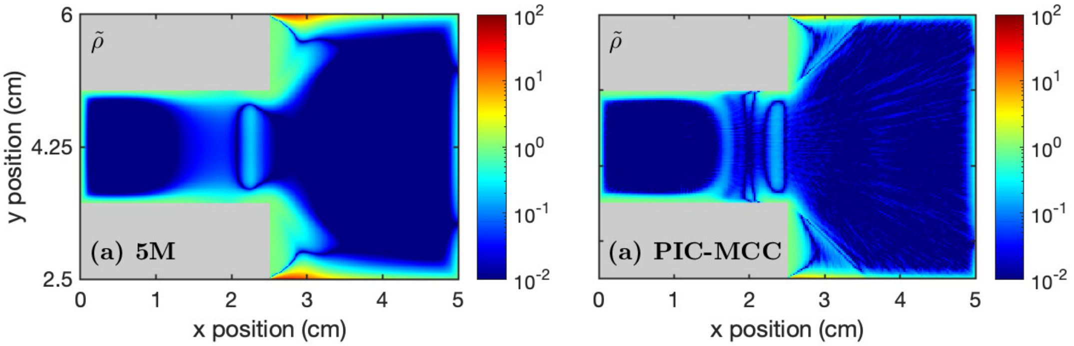

Figure 6. A comparison between the normalized space charge density in the (a) 5M and (b) PIC-MCC simulations.

electron current density is largely due to the differences in electron density, rather than azimuthal velocity.

Figure 6 compares the normalized space charge density between the 5M and PIC-MCC results, computed as

$$\tilde{\rho} = \left| \frac{n_i - n_e}{n_i} \right| . \tag{52}$$

Good qualitative agreement can be seen throughout much of the domain, with deviations primarily occurring near $x = 2$ cm, corresponding to the location of the inverse sheath discussed previously, and in front of the pole piece where the non-neutral region in the 5M result extends farther into the plume. The similar sheath structure supports the hypothesis that similar non-neutral moment models may be a valuable tool in understanding electron transport in these regions.

VIII. Results: Thermal conductivity study

As was demonstrated in Sec. VII, a major source of disagreement between the 5M and PIC-MCC results is in the electron temperature profile, which can be attributed to either an over-predicted field aligned heat flux or reduced cross-field heat flux. Because the most commonly used conductive heat flux description for fluid HET models is Fourier's law, given in Eq. (25), we have conducted a sensitivity study where the field aligned thermal conductivity is modified independent of the cross-field heat flux. If the collision frequency in the denominator of Eq. (27) is viewed as the heat-exchange collision frequency, $\nu_{e,q} = \nu_{e,m}/\alpha_q$, rather than momentum exchange collision frequency, then a reduction of the thermal conductivity can be viewed as an increase in this heat-exchange frequency. Here, we compare simulations with $\alpha_q = 1, 10, 100$, and 200. The discharge current does not appear to change with thermal conductivity. Further reducing $\kappa_\parallel$ was found to lead to large amplitude current pulses due to the the neutral density reaching a value of zero during the transient phase of the simulation, which is a limitation of the simplified, quasi-steady model for neutral atoms.

Figure 7 shows contour plots of the ion density, electron density, electron temperature, and plasma potential for the cases of $\alpha_q = 1, 10, 100$, and 200, respectively. Figure 8 compares the centerline electron number density, neutral number density, ion axial bulk velocity, electron temperature, plasma potential, axial electric field, electron axial bulk velocity, and electron azimuthal bulk velocity of the four cases to the PIC-MCC results. In Figs. 7 (a)-(h), as well as Fig. 8(a), it can be seen that peak plasma density increases and moves closer to the anode. Correspondingly, the peak neutral number density in Fig. 8(b) increases near the anode and the neutral density in the bump around $x = 2.5$ cm increases. As the neutral density in the bump increases, so does the ionization rate, which leads to the production of more slow ions and decreases the axial ion bulk velocity in the dip at $x = 2.8$ cm, shown in Fig. 8(c), without affecting the peak velocity at $x = 2.3$ cm.

Figures 7(i)-(l) and Fig. 8(d) show that the peak electron temperature increases as $\kappa_\parallel$ decreases and the field lines become increasingly non-isothermal. Although reducing $\kappa_\parallel$ brings the 5M model electron temperature profile into closer agreement with that of the PIC-MCC model in the downstream region of

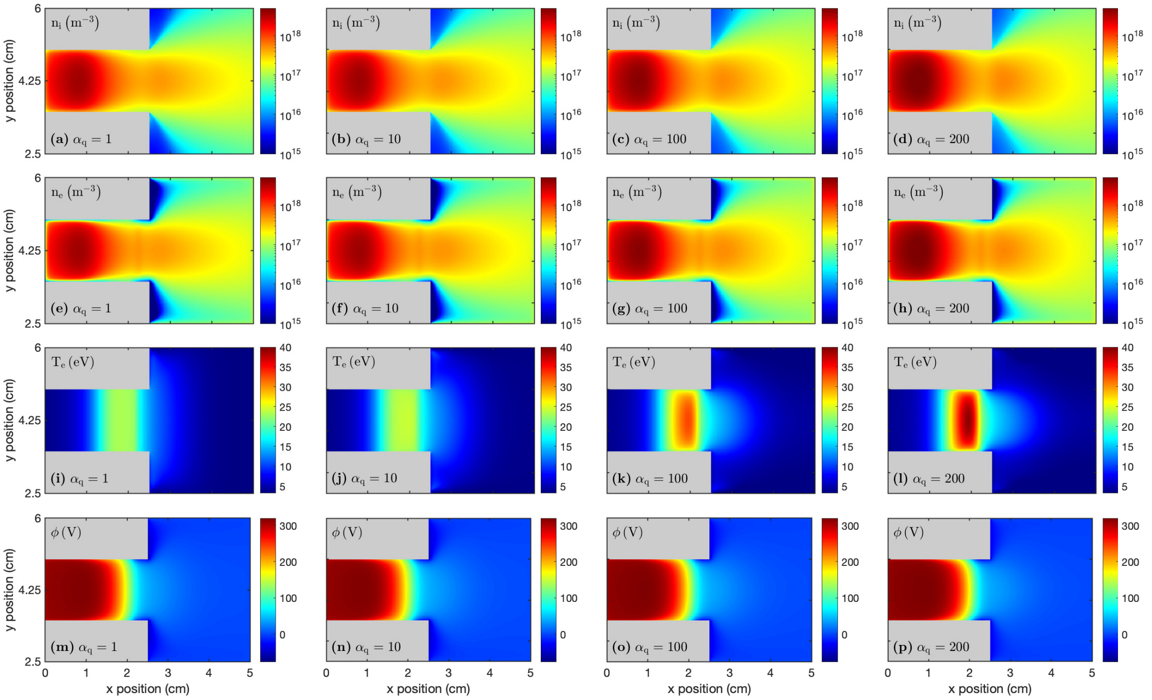

Figure 7. Two-dimensional contour plots of selected plasma properties from the 5M results with varying $\kappa_\parallel$.

the discharge channel, the effects of the anisotropic pressure tensor are still absent. It can also be seen that additional electron heating occurs in front of the pole piece due to the stretching of the electron VDF in the sheath, i.e., $\vec{u}_e \cdot \nabla T_e > 0$.

Figures 7(m)-(p) and Fig. 8(d) show that the changes to the plasma potential are more subtle. The peak plasma potential increases slightly with reduced $\kappa_\parallel$, reaching 320 V at $\alpha_q = 200$, which leads to a more negative electric field at the anode, shown in Fig. 8(e). Correspondingly, there is a decrease in the cross-field electron velocity towards the anode, shown in Fig. 8(f). The acceleration region also steepens, leading to the increased axial electric field shown in Fig. 8(e) and azimuthal electron drift velocity in Fig. 8(g).

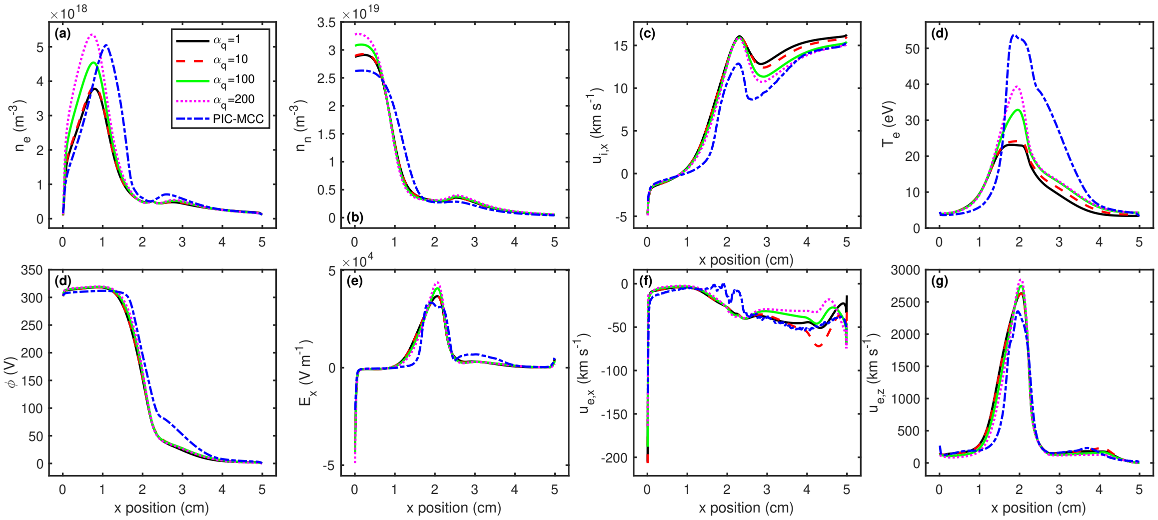

Figure 8. Centerline plots of selected plasma properties with varying $\kappa_\parallel$ from the 5M results compared to the PIC-MCC results.

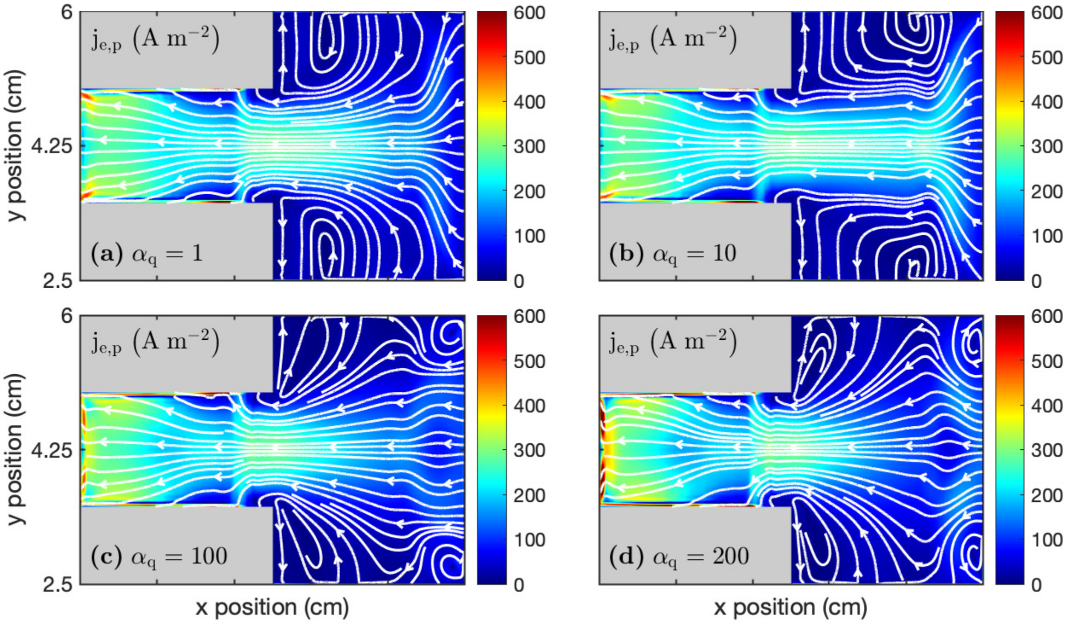

Figure 9. 2D contour plots of the planar electron current density with varying $\kappa_\parallel$ from the 5M results.

The planar electron current densities for $\alpha_q = 1$, 10, 100, and 200 are shown in Figs. 9(a)-(d), respectively. The agreement between the 5M and PIC-MCC results in the plume worsens considerably with reduced $\kappa_\parallel$, with the recirculation region moving from its original location of $x = 3.2$ cm to the downstream corners of the domain before eventually reforming as a second vortical structure. In accordance with Fig. 8(f), the axial electron bulk velocity becomes less negative in the far-field plume, leading to a shortened high current density region just outside the channel exit. Within the discharge channel, significant changes are visible near the anode, where in accordance with Figs. 8(a) and (f), the electron current density increases near the channel centerline and moves away from the two-lobed profile visible in the $\alpha_q = 1$ and PIC-MCC results. Although the contours are not shown here, as can be inferred from Fig. 8(g), the peak azimuthal electron current density increases with reduced $\kappa_\parallel$.

Although reducing the field-aligned thermal conductivity has the intended effect of reducing isothermality of the magnetic field lines, it is clear that when taking a wholistic view of the plasma response this causes greater deviations from the kinetic results in many other aspects of the discharge, especially the electron velocity. However, such a modification may be appropriate within the downstream region of the discharge channel, where the primary effect was to reduce field line isothermality without strongly affecting the electron properties. These results highlight that a more careful examination of the heat flux closure used in HET modeling is necessary and that ad-hoc modifications to the effective electron scattering frequency using a Fourier law are insufficient to produce agreement between kinetic and fluid models.

IX. Conclusions

In this paper, we have presented a a two-dimensional, axial-radial, five-moment fluid model for a Hall effect thruster and benchmarked it against results from a particle-in-cell Monte Carlo collision model. Unlike the majority of HET models in the literature, the presented model is non-neutral and retains electron inertial effects. The model also uses a non-isothermal multi-fluid model for the ions which can produce good qualitative agreement with the ion velocity profiles from the PIC-MCC results. Good qualitative agreement is observed between the 5M and PIC-MCC models throughout much of the discharge plasma. The largest deviations between the two models appear to be driven by the details of the plasma sheaths, where the electron VDF is expected to most strongly deviate from a Maxwellian, and the electron conductive heat flux, which is zero for a Maxwellian VDF and must be informed by higher-order closures to the fluid equations.

The use of Fourier's law for the conductive heat flux in the 5M model is found to cause highly isothermal field lines which are not observed in the kinetic results. Through a sensitivity study, we have demonstrated that reducing the field-aligned thermal conductivity can bring the mean temperature profiles of the two models into closer agreement but leads to worse agreement in the electron density and velocity. This suggests that modifying the effective thermal conductivity is insufficient to explain the electron heat flux in HET plasmas and motivates a deeper study into higher-order heat flux closures, to be completed in future work. We also plan to apply the model to a more realistic magnetic field topology, which will enable a more direct comparison with existing numerical results and experimental measurements.

X. Acknowledgements

This work was supported by a NASA Space Technology Graduate Research Opportunity and by NASA through the Joint Advanced Propulsion Institute, a NASA Space Technology Research Institute under Grant No. 80NSSC21K1118. Some of the computing for this project was performed on the Sherlock cluster. We would like to thank Stanford University and the Stanford Research Computing Center for providing computational resources and support that contributed to these research results.

References

[1] J. M. Fife, *Two-Dimensional Hybrid Particle-In-Cell Modeling of Hall Thrusters.* PhD thesis, Massachusetts Institute of Technology, Cambridge, MA, 1995.

[2] I. G. Mikellides and I. Katz, "Numerical simulations of Hall-effect plasma accelerators on a magnetic-field-aligned mesh," *Phys. Rev. E*, vol. 86, p. 046703, Oct 2012.

[3] A. Domínguez Vázquez, *Axisymmetric simulation codes for Hall effect thrusters and plasma plumes.* PhD thesis, Universidad Carlos III de Madrid, Leganés, Spain, 2019.

[4] K. Hara, "An overview of discharge plasma modeling for Hall effect thrusters," *Plasma Sources Science and Technology*, vol. 28, no. 4, p. 044001, 2019.

[5] R. Sahu, A. R. Mansour, and K. Hara, "Full fluid moment model for low temperature magnetized plasmas," *Physics of Plasmas*, vol. 27, 11 2020. 113505.

[6] D. A. Kuldinow, Y. Yamashita, and K. Hara, "Ten-moment fluid model for low-temperature magnetized plasmas," *Physics of Plasmas*, vol. 31, no. 12, p. 123506, 2024.

[7] Y. Yamashita, R. Lau, and K. Hara, "Inertial and anisotropic pressure effects on cross-field electron transport in low-temperature magnetized plasmas," *Journal of Physics D: Applied Physics*, vol. 56, p. 384003, jun 2023.

[8] T. Charoy, J.-P. Boeuf, A. Bourdon, J. A. Carlsson, P. Chabert, B. Cuenot, D. Eremin, L. Garrigues, K. Hara, I. D. Kaganovich, *et al.*, "2d axial-azimuthal particle-in-cell benchmark for low-temperature partially magnetized plasmas," *Plasma Sources Science and Technology*, vol. 28, no. 10, p. 105010, 2019.

[9] W. Villafana, B. Cuenot, and O. Vermorel, "3D particle-in-cell study of the electron drift instability in a Hall Thruster using unstructured grids," *Physics of Plasmas*, vol. 30, p. 033503, 03 2023.

[10] A. I. Morozov, "The conceptual development of stationary plasma thrusters," *Plasma Physics Reports*, vol. 29, pp. 235–250, 2003.

[11] I. D. Kaganovich, Y. Raitses, D. Sydorenko, and A. Smolyakov, "Kinetic effects in a Hall thruster dischargea)," *Physics of Plasmas*, vol. 14, p. 057104, 05 2007.

[12] A. Marín-Cebrián, E. Bello-Benítez, A. Domínguez-Vázquez, and E. Ahedo, "Non-Maxwellian electron effects on the macroscopic response of a Hall thruster discharge from an axial–radial kinetic model," *Plasma Sources Science and Technology*, vol. 33, no. 2, p. 025008, 2024.

[13] A. Lopez Ortega and I. G. Mikellides, "A new cell-centered implicit numerical scheme for ions in the 2-D axisymmetric code Hall2De," in *50th AIAA/ASME/SAE/ASEE Joint Propulsion Conference*, p. 3621, 2014.

[14] H. Liu, B. Wu, D. Yu, Y. Cao, and P. Duan, "Particle-in-cell simulation of a Hall thruster," *Journal of Physics D: Applied Physics*, vol. 43, no. 16, p. 165202, 2010.

[15] H.-W. Drawin, "Zur formelmäßigen darstellung der ionisierungsquerschnitte gegenüber elektronenstoß," *Zeitschrift für Physik*, vol. 164, no. 5, pp. 513–521, 1961.

[16] M. Mitchner and C. H. Kruger, Jr., *Partially ionized gases.* John Wiley and Sons, Inc., New York, 1973.

[17] I. G. Mikellides, A. Lopez Ortega, and V. H. Chaplin, "Theory of the anomalous momentum exchange from wave–particle interactions in Hall-effect ion accelerators and comparisons with measurements," *Physics of Fluids*, vol. 36, p. 074121, 07 2024.

[18] K. Hara and I. G. Mikellides, "Characterization of low frequency ionization oscillations in Hall thrusters using a one-dimensional fluid model," in *2018 Joint Propulsion Conference*, p. 4904, 2018.

[19] J. S. Miller, S. H. Pullins, D. J. Levandier, Y.-h. Chiu, and R. A. Dressler, "Xenon charge exchange cross sections for electrostatic thruster models," *Journal of Applied Physics*, vol. 91, no. 3, pp. 984–991, 2002.

[20] M. Campanell, A. Khrabrov, and I. Kaganovich, "Instability, collapse, and oscillation of sheaths caused by secondary electron emission," *Physics of Plasmas*, vol. 19, no. 12, 2012.

[21] M. Campanell, A. Khrabrov, and I. Kaganovich, "General cause of sheath instability identified for low collisionality plasmas in devices¡? format?¿ with secondary electron emission," *Physical review letters*, vol. 108, no. 23, p. 235001, 2012.

[22] K. Hara, *Development of Grid-Based Direct Kinetic Method and Hybrid Kinetic-Continuum Modeling of Hall Thruster Discharge Plasmas.* PhD thesis, University of Michigan, 2015.

[23] S. Gottlieb, C.-W. Shu, and E. Tadmor, “Strong stability-preserving high-order time discretization methods,” *SIAM review*, vol. 43, no. 1, pp. 89–112, 2001.

[24] B. Van Leer, “Towards the ultimate conservative difference scheme. V. a second-order sequel to Godunov’s method,” *Journal of computational Physics*, vol. 32, no. 1, pp. 101–136, 1979.

[25] J. L. Steger and R. Warming, “Flux vector splitting of the inviscid gasdynamic equations with application to finite-difference methods,” *Journal of computational physics*, vol. 40, no. 2, pp. 263–293, 1981.

[26] J. P. Boris, “Acceleration calculation from a scalar potential,” tech. rep., Princeton Plasma Physics Laboratory, 12 1969.

[27] C. K. Birdsall and D. Fuss, “Clouds-in-clouds, clouds-in-cells physics for many-body plasma simulation,” *Journal of Computational Physics*, vol. 3, no. 4, pp. 494–511, 1969.

[28] H. R. Skullerud, “The stochastic computer simulation of ion motion in a gas subjected to a constant electric field,” *Journal of Physics D: Applied Physics*, vol. 1, p. 1567, nov 1968.

[29] “*hypre*: High performance preconditioners.” `https://llnl.gov/casc/hypre`, `https://github.com/hypre-space/hypre`.

[30] I. D. Boyd, D. B. Van Gilder, and X. Liu, “Monte Carlo simulation of neutral xenon flows in electric propulsion devices,” *Journal of propulsion and power*, vol. 14, no. 6, pp. 1009–1015, 1998.

[31] J. Sheehan, I. Kaganovich, H. Wang, D. Sydorenko, Y. Raitses, and N. Hershkowitz, “Effects of emitted electron temperature on the plasma sheath,” *Physics of Plasmas*, vol. 21, no. 6, 2014.

[32] J. L. S. Betancourt, N. Butler-Craig, J. Lopez-Uricoechea, A. M. Steinberg, and M. L. Walker, “Laser thomson scattering measurements indicate non-isothermal magnetic field lines in magnetically shielded hall effect thrusters,” *Physics of Plasmas*, vol. 31, no. 11, 2024.

[33] P. J. Roberts, M. G. Allen, D. G. Brick, and B. A. Jorns, “Empirical closures for momentum and energy transport in hall thrusters based on thomson scattering measurements,” in *38th Int. Electric Propulsion Conf.(Electric Rocket Society, Toulouse, 2024)*, 2024.

[34] A. Marín-Cebrián, E. Ahedo, and A. Domínguez-Vázquez, “Two-dimensional kinetic analysis of a Hall thruster discharge with a null-magnetic point at the anode,” *Journal of Physics D: Applied Physics*, 2025.

[35] A. M. Castillo and K. Hara, “Loss cone effects and monotonic sheath conditions of a partially magnetized plasma sheath,” *Physics of Plasmas*, vol. 31, no. 3, 2024.